nature machine intelligence

SUPPLEMENTARY INFORMATION

https://doi.org/10.1038/s42256-019-0044-1

In the format provided by the authors and unedited.

Distributed sensing for fluid disturbance compensation and motion control of intelligent robots

Michael Krieg[1,2], Kevin Nelson[2,3] and Kamran Mohseni[1,2,3]*

[1]University of Florida, Mechanical and Aerospace Engineering, Gainesville, FL, USA. [2]University of Florida, Institute for Networked Autonomous Systems, Gainesville, FL, USA. [3]University of Florida, Electrical and Computer Engineering, Gainesville, FL, USA. *e-mail: mohseni@ufl.edu

Supplementary Materials to the Paper, "Distributed sensing for fluid disturbance compensation and motion control of intelligent robots"

This document contains additional information about subsystems, calibration procedures, theoretical analysis, and peripheral results that were not necessary to elucidate the central message of the paper, but might be of interest to readers. This supplemental contains the following sections:

Supplementary Figures

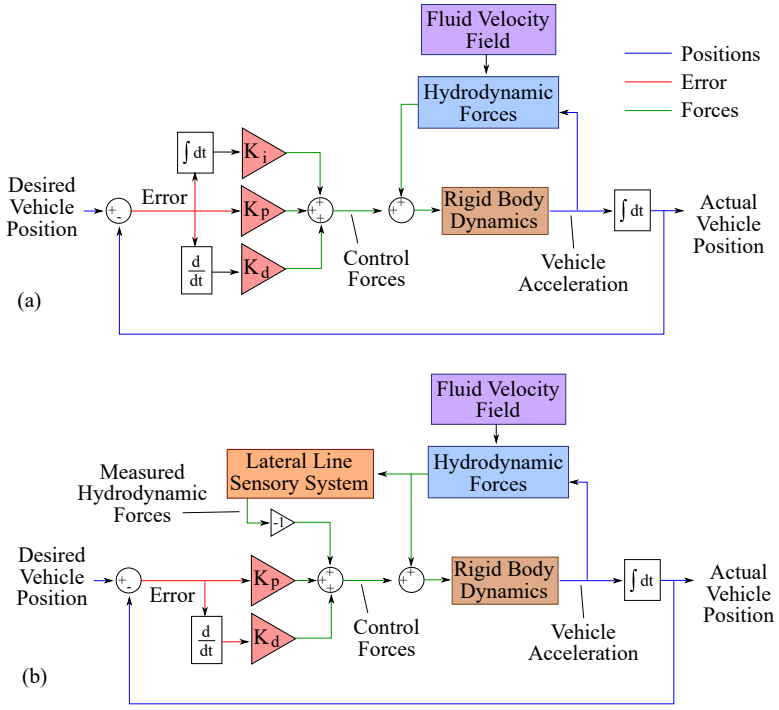

Supplementary Figure 1: Block diagrams showing possible autonomous vehicle motion controllers, including (a) a standard PID controller, and (b) a disturbance force feedforward controller made possible by the lateral line inspired sensory system.

Supplementary Discussion

Comparison of Static and Dynamic Forces

One important feature of this study is development of a technique to isolate dynamic fluid forces, corresponding to disturbances, from static ones, corresponding to buoyancy forces, which is described in detail in the **Methods** section. For the neutrally buoyant vehicle, the weight force is equal to the buoyancy force and both are aligned with the inertial Z-axis. As the vehicle attitude shifts, the projection of the buoyancy and weight forces onto the body fixed sway axis becomes non-zero. Since the buoyancy force is already being balanced by the weight force, any component in the sway direction would not need to be compensated by the feedforward controller.

The static pressure distribution over the vehicle can be integrated to produce the buoyancy forces acting on the vehicle. Due to the increased hydrostatic pressure at the base of the vehicle, the buoyancy force is in the positive inertial z direction, when at rest, which is in equilibrium with the weight force for this neutrally buoyant vehicle. When the vehicle experiences nonzero roll or pitch, the inertial z-axis and body fixed z-axis are no longer aligned, causing the buoyant force to have nonzero components along other body axes. Since the buoyancy force is already being balanced by the weight force, any component in the sway direction would not need to be compensated by the feedforward controller. Here we will discuss relative magnitudes of the static pressure force component to illustrate how important this process is to the overall force compensation technique.

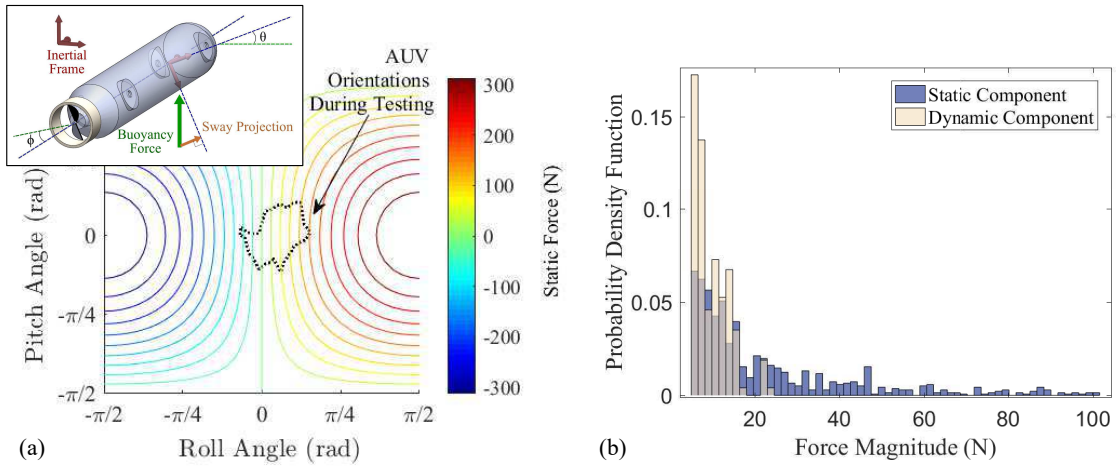

Supplementary Figure 2: (a) Contour of the buoyancy force aligned in the sway axis as a function of the roll and pitch angles of the vehicle. The dashed line shows the region of operation of the vehicle during the various tests reported in this study. (b) Histogram of the absolute value of the component of the buoyant force aligned with the sway axis of the vehicle. The graph is normalized such that the bins of the histogram represent the probability distribution of the data.

As part of the hydrodynamic force estimation algorithm, we provided calculations for the total hydrodynamic force on a vehicle in terms of Fourier coefficients of a periodic pressure distribution over the surface, summarized by equations (12) and (14). Given the vehicle cylindrical shape, and the linear increase in hydrostatic pressure with depth, the static pressure difference across any set of differential ports can be written in terms of the roll angle, θ, pitch angle, ϕ, AUV radius, R, fluid density, ρ, angular position of the sensor module, γ, and angular separation of the sensor ports, α.

$$\begin{aligned}\Delta P_s = \rho R \cos\theta \Big(\cos\phi \Big[\cos\Big(\gamma + \frac{\alpha}{2}\Big) - \cos\Big(\gamma - \frac{\alpha}{2}\Big)\Big] \\ - \sin\phi \Big[\sin\Big(\gamma + \frac{\alpha}{2}\Big) - \sin\Big(\gamma - \frac{\alpha}{2}\Big)\Big]\Big)\,.\end{aligned} \tag{1}$$

This expression for the pressure difference of just the static component can be rearranged into the form of a Fourier series in θ (9) with the following coefficients,

$$a_{1s} = -\rho g R \cos\phi \cos\theta\,, \quad b_{1s} = \rho g R \sin\phi \cos\theta\,. \tag{2}$$

Here, ρ is the fluid density, R is the AUV radius, and g is gravitational acceleration. For a vehicle of length L, this corresponds to a force (14) in the sway direction corresponding to a component of the buoyancy force of,

$$F_s = \rho g L \pi R^2 \cos\phi \cos\theta\,. \tag{3}$$

Supplementary Fig. 2a shows a contour plot of the magnitude of static sway force at different roll and pitch angles. The maximum and minimum forces are ± 345 N and occur at pitch angles of 0 radians and roll angles of $\pm\pi$ radians, respectively. This is equivalent to the vehicle orientation such that the buoyant force is entirely aligned along the body y-axis.

Additionally, Supplementary Figure 2a shows the operational region of the vehicle (indicated by a dashed line) during the data-sets reported in this study. As is shown in the figure, there are times when the vehicle operates near roll angles of $30°$, corresponding to sway forces well over 100 N, which are much larger than the typical

dynamic forces experienced from the disturbance generator. To illustrate this more quantitatively, Supplementary Figure 2b shows a probability histogram of the absolute value of the component of buoyancy force in the sway axis in addition to the histogram of all dynamic forces experienced by the vehicle in that axis. As can be observed from the histogram the vast majority of dynamic forces occur below 18 N; whereas, the static force has a significant probability of occurring at the higher forces, some of them double or triple the range of dynamic forces experienced.

This analysis demonstrates how an accurate method of removing the static pressure/buoyancy force from the lateral line measurements is necessary for successful hydrodynamic force compensation, as even small changes in attitude can produce large buoyancy forces in the sway direction which are already compensated by the weight force. Since the vehicle used in this study is free to move in all 6 DOF, like an AUV operating in the field, and does not have active roll and pitch control (it is passively stable) we require an accurate estimate of the vehicle attitude. However, AUV attitude is typically easier to measure from inertial sensors than position.

Additional Controller Analysis

This supplemental section provides additional discussion on controllers for AUVs and presents the stability analysis of the motion controllers. Some equations are replicated for clarity.

There have been some studies examining partial differential equation based underwater vehicle controllers which use fluid environmental data to create short term predictions of hydrodynamic interactions [1, 2]. The use of this type of controller is extremely limited, and requires extensive infrastructure to monitor and interpolate fluid environmental conditions. Advances have been made towards characterizing material transport dynamics within complex large scale ocean flows through the use of Lagrangian coherent structures (LCS) analysis [3, 4, 5]. By identifying attracting and repelling material transport boundaries, and the propagation of those boundaries, higher level navigation controllers can place the vehicle into a region such that the surrounding fluid helps to eventually carry the vehicle close to the final target location, albeit through an often convoluted path to that desired point. This type of navigational control can greatly reduce total fuel consumption during transit, but is based on the principal of moving with the flow in an intelligent sense. Hence, LCS analysis does little to help a vehicle that is trying to maintain a stationary position after reaching its destination.

Other controllers approach fluid disturbances from a probabilistic standpoint. Techniques that take into account the effect of noise on controller dynamic switching [6, 7] have been applied to underwater vehicle navigation [8]. This technique allows the controller to identify probable escape trajectories, but again does little to help a vehicle maintain a desired position prior to being displaced by a disturbance/noise.

PD Controller

The analysis in this section shows how disturbances in the fluid environment affect vehicle controller stability and show specific advantages of the force feedforward approach. Proportional-derivative (PD) and proportional-integral-derivative (PID) feedback controllers are used as basic, well understood examples to help illustrate the effect of disturbances on controller stability and the simplest method of dealing with those disturbances. As was mentioned previously, there are an abundance of more complicated controllers to address the issue of disturbances. In a following section we will discuss the relative performance of sliding mode and adaptive sliding controllers through the use of a one DOF simulation. Although deriving the full 6 DOF stability analysis of these controllers is beyond the scope of this work, the one DOF stability is implied by the controller definition, as will be seen. We invite the interested reader to consult [9] for a more thorough summary. Furthermore, many of the modern control techniques rely on vehicle kinematics based models of hydrodynamic forces (see equation (2) in the main text), which requires experimental characterization of all the drag and added mass coefficients which has not been done for this AUV. Both the PID and new feedforward/PD control algorithms are shown in block diagram form in Supplemental Fig. 1 to help illustrate the new control strategy.

We first define a standard PD controller and show that it loses stability in the presence of a uniform disturbance, motivating the use of an integral term. However, the PID controller is not stable to arbitrary disturbances.

Finally, we demonstrate that a controller which combines a hydrodynamic force feedforward term with a simple PD feedback term is capable of providing stability in the presence of arbitrary disturbances. Initially, consider vehicle dynamics without disturbances modeled by the following equations,

$$M\dot{\boldsymbol{\nu}} + C(\boldsymbol{\nu})\boldsymbol{\nu} + D(\boldsymbol{\nu})\boldsymbol{\nu} + G(\boldsymbol{\eta}) = \boldsymbol{\tau}, \tag{4a}$$

$$\dot{\boldsymbol{\eta}} = J(\boldsymbol{\eta})\boldsymbol{\nu}, \tag{4b}$$

where the vector $\boldsymbol{\eta} \in \mathbb{R}^n$ contains the position and orientation of the vehicle in the inertial frame and $\boldsymbol{\nu} \in \mathbb{R}^n$ contains the linear and angular velocity of the vehicle expressed in the body-fixed frame with n representing the number of states. $M \in \mathbb{R}^{n\times n}$ is a matrix containing the inertial terms of the rigid body, $C : \mathbb{R}^n \to \mathbb{R}^{n\times n}$ is a matrix containing the Coriolis/centrifugal terms of the rigid body, which is a function of the body rotational velocities, $D : \mathbb{R}^n \to \mathbb{R}^{n\times n}$ represents the drag terms, $G : \mathbb{R}^n \to \mathbb{R}^n$ represents the restoring forces, the vector $\boldsymbol{\tau} \in \mathbb{R}^n$ denotes the control forces and moments, and $J : \mathbb{R}^n \to \mathbb{R}^{n\times n}$ represents the velocity transformation from the body-fixed frame to the inertial frame. The system has the following properties:

Property 1: The matrix M is positive definite.
Property 2: The matrix $C(\nu)$ is skew symmetric.
Property 3: The matrix $D(\nu)$ is positive definite.
Property 4: The matrix $J(\eta)$ is orthogonal.

To simplify the problem, we limit the dynamics to three degrees of freedom (DOF) and assume that the vehicle is neutrally buoyant and roll and pitch stable. This implies that the gravitational and restoring forces can be neglected, i.e. $G(\boldsymbol{\eta}) = 0$. For station keeping, the desired trajectory, $\boldsymbol{\eta_d}$, is a fixed point in space. We can define an error system as

$$\boldsymbol{e_1} = \boldsymbol{\eta_d} - \boldsymbol{\eta}, \tag{5}$$

and the derivative of the error is denoted e_2. Designing the feedback controller as

$$\boldsymbol{\tau} = J^{-1}(\boldsymbol{\eta})\left(K_p\boldsymbol{e_1} + K_d\boldsymbol{e_2}\right), \tag{6}$$

where $K_p, K_d \in R^{n\times n}$ are diagonal matrices of positive, constant gains.

Theorem S1: The controller given by (6) exponentially stabilizes the system (4), in the sense that

$$\|\boldsymbol{e_1}\| \to 0 \quad \text{as} \quad t \to \infty,$$

given sufficient choices of gains K_p and K_d that satisfy

$$\lambda_{min}(K_p) > \frac{1}{2}, \quad (\lambda_{min}(D^*) + \lambda_{min}(K_d)) > \frac{1}{2}, \tag{7}$$

where where $\lambda_{min}(\cdot)$ denotes the minimum eigenvalue of the matrix and D^* is defined below.

Proof: To aid analysis, we can rewrite the state equation (4) as

$$M^*(\boldsymbol{\eta})\ddot{\boldsymbol{\eta}} + C^*(\boldsymbol{\nu},\boldsymbol{\eta})\dot{\boldsymbol{\eta}} + D^*(\boldsymbol{\nu},\boldsymbol{\eta})\dot{\boldsymbol{\eta}} = J(\boldsymbol{\eta})\boldsymbol{\tau}, \tag{8}$$

where

$$M^*(\boldsymbol{\eta}) = J(\boldsymbol{\eta})MJ^{-1}(\boldsymbol{\eta}),$$
$$C^*(\boldsymbol{\nu},\boldsymbol{\eta}) = J(\boldsymbol{\eta})[C(\boldsymbol{\nu}) - MJ^{-1}(\boldsymbol{\eta})\dot{J}(\boldsymbol{\eta})]J^{-1}(\boldsymbol{\eta}).$$
$$D^*(\boldsymbol{\nu},\boldsymbol{\eta}) = J(\boldsymbol{\eta})D(\boldsymbol{\nu})J^{-1}(\boldsymbol{\eta}).$$

It can be shown that the matrix $\frac{1}{2}\dot{M}^* - C^*$ is skew-symmetric and M^* and D^* are positive definite [10].

Pre-multiplying the error system by the inertial matrix gives

$$M^*\dot{\boldsymbol{e_2}} = -M^*\ddot{\boldsymbol{\eta}} = C^*\dot{\boldsymbol{\eta}} + D^*\dot{\boldsymbol{\eta}} - J(\boldsymbol{\eta})\boldsymbol{\tau}. \tag{10}$$

We choose a Lyapunov function candidate as

$$V = \frac{1}{2}\boldsymbol{e_1}^T\boldsymbol{e_1} + \frac{1}{2}\boldsymbol{e_2}^T M^*\boldsymbol{e_2}. \tag{11}$$

Then its derivative is

$$\begin{aligned}\dot{V} =& \boldsymbol{e_1}^T\dot{\boldsymbol{e}}_1 + \boldsymbol{e_2}^T M^*\dot{\boldsymbol{e}}_2 + \frac{1}{2}\boldsymbol{e_2}^T\dot{M}^*\boldsymbol{e_2}, \\ =& \boldsymbol{e_1}^T\boldsymbol{e_2} + \boldsymbol{e_2}^T(C^*\dot{\boldsymbol{\eta}} + D^*\dot{\boldsymbol{\eta}} - J(\boldsymbol{\eta})\boldsymbol{\tau}) + \frac{1}{2}\boldsymbol{e_2}^T\dot{M}^*\boldsymbol{e_2}.\end{aligned} \tag{12}$$

Exploiting the skew-symmetry property of $\frac{1}{2}\dot{M}^* - C^*$ and plugging (6) into (12) gives

$$\dot{V} = \boldsymbol{e_1}^T\boldsymbol{e_2} - \boldsymbol{e_2}^T K_p\boldsymbol{e_1} - \boldsymbol{e_2}^T D^*\boldsymbol{e_2} - \boldsymbol{e_2}^T K_d\boldsymbol{e_2}. \tag{13}$$

Applying Young's inequality gives us

$$\begin{aligned}\dot{V} \leq& \left(\frac{1}{2} - \lambda_{min}(K_p)\right)\|\boldsymbol{e_1}\|^2 \\ &+ \left(\frac{1}{2} - \lambda_{min}(D^*) - \lambda_{min}(K_d)\right)\|\boldsymbol{e_2}\|^2.\end{aligned} \tag{14}$$

Assuming K_p and K_d are chosen such that (7) is satisfied, $\dot{V}$ is negative definite, and since V is a positive definite function, it follows from Theorem 4.10 of [11] that the equilibrium point $\boldsymbol{e_1} = 0$ is globally exponentially stable. □

Though the PD controller can be shown to stabilize the vehicle without disturbances, it can be shown that in a constant flow, the PD controller will only achieve a uniformly bounded result. That is, the vehicle will reach a position where the inertial velocity is zero and the proportional error control force reaches an equilibrium with the drag force created by the background flow.

The failings of the PD controller to maintain position tracking stability in the presence of disturbances motivates the development of an integral term. That is, designing the controller as

$$\tau = J^{-1}(\boldsymbol{\eta})\left(K_p\boldsymbol{e_1} + K_d\boldsymbol{e_2} + K_i\int_0^t \boldsymbol{e_1}(\sigma)d\sigma\right). \tag{15}$$

Given enough control authority and time, the integral term will eventually overcome the background flow, causing the controller to converge to the set point. However, it takes time for the integral term to build up and overcome the disturbance and the integral term only guarantees tracking stability for certain classes of disturbances, such as constant current. This motivates the use of a distributed sensory system to directly measure the disturbances.

PD Controller with Hydrodynamic Force Feedforward

The most general formulation of underwater vehicle dynamics is given by the governing equations for a rigid body, with an additional term for hydrodynamic forces,

$$M_{RB}\dot{\boldsymbol{\nu}} + C_{RB}(\boldsymbol{\nu})\boldsymbol{\nu} + \boldsymbol{F_d} = \boldsymbol{\tau}, \tag{16a}$$

$$\dot{\boldsymbol{\eta}} = J(\boldsymbol{\eta})\boldsymbol{\nu}, \tag{16b}$$

where the vector $\boldsymbol{\eta} \in \mathbb{R}^n$ contains the position and orientation of the vehicle in the inertial frame and $\boldsymbol{\nu} \in \mathbb{R}^n$ contains the linear and angular velocity of the vehicle expressed in the body-fixed frame with n representing the number of states. $M_{RB} \in \mathbb{R}^{n\times n}$ is a matrix containing the inertial terms of the rigid body, $C_{RB} : \mathbb{R}^n \to \mathbb{R}^{n\times n}$ is a matrix containing the Coriolis/centrifugal terms of the rigid body, which is a function of the body rotational velocities, $\boldsymbol{F_d} \in \mathbb{R}^n$ represents the vector of fluid forces acting on the vehicle, the vector $\boldsymbol{\tau} \in \mathbb{R}^n$ denotes the control forces and moments, and $J : \mathbb{R}^n \to \mathbb{R}^{n\times n}$ represents the velocity transformation from the body-fixed frame to the inertial frame.

Assumption 1: The hydrodynamic forces, $\boldsymbol{F_d}$, can be accurately measured and are bounded such that they do not exceed the control authority of the system.

Provided Assumption 1 holds, a controller can be designed as

$$\boldsymbol{\tau} = \boldsymbol{F_d} + \boldsymbol{\tau_{FB}}, \tag{17}$$

where $\boldsymbol{\tau_{FB}} \in \mathbb{R}^n$ is a stabilizing error feedback controller with the assumption that the sum of the feedforward and feedback signals does not exceed the thruster capacity. After inserting (17) into (16a), the complexity of the control problem is reduced to the control of a rigid body in a vacuum under a given external forcing,

$$M_{RB}\dot{\boldsymbol{\nu}} + C_{RB}(\boldsymbol{\nu})\boldsymbol{\nu} = \boldsymbol{\tau_{FB}}. \tag{18}$$

Theorem 1: If Assumption 1 is satisfied, then the controller given by (17) with feedback controller (6) exponentially stabilizes the system (16) in the sense that

$$\|\boldsymbol{e_1}\| \to 0 \quad \text{as} \quad t \to \infty,$$

assuming sufficient choices of gains K_p and K_d that satisfy

$$\lambda_{min}(K_p) > \frac{1}{2}, \quad \lambda_{min}(K_d) > \frac{1}{2}. \tag{19}$$

Proof: Similar to the previous analysis, we can rewrite the state equation (18) as

$$M^*_{RB}(\boldsymbol{\eta})\ddot{\boldsymbol{\eta}} + C^*_{RB}(\boldsymbol{\nu},\boldsymbol{\eta})\dot{\boldsymbol{\eta}} = J(\boldsymbol{\eta})\boldsymbol{\tau_{FB}}, \tag{20}$$

where

$$M^*_{RB}(\boldsymbol{\eta}) = J(\boldsymbol{\eta})M_{RB}J^{-1}(\boldsymbol{\eta}),$$
$$C^*_{RB}(\boldsymbol{\nu},\boldsymbol{\eta}) = J(\boldsymbol{\eta})[C_{RB}(\boldsymbol{\nu}) - M_{RB}J^{-1}(\boldsymbol{\eta})\dot{J}(\boldsymbol{\eta})]J^{-1}(\boldsymbol{\eta}),$$

where again the matrix $\frac{1}{2}\dot{M}^*_{RB} - C^*_{RB}$ is skew-symmetric and M^*_{RB} is positive definite.

If we choose the Lyapunov function candidate

$$V = \frac{1}{2}\boldsymbol{e_1}^T\boldsymbol{e_1} + \frac{1}{2}\boldsymbol{e_2}^T M^*\boldsymbol{e_2}\,, \tag{22}$$

and the feedback controller (6), we can use similar techniques as before to show that an upper bound of the derivative of the Lyapunov function candidate is given by

$$\dot{V} \leq \left(\frac{1}{2} - \lambda_{min}(K_p)\right)\|\boldsymbol{e_1}\|^2 + \left(\frac{1}{2} - \lambda_{min}(K_d)\right)\|\boldsymbol{e_2}\|^2\,.$$

If K_p and K_d are chosen such that (19) is satisfied, then $\dot{V}$ is negative definite, and since V is a positive definite function, it follows from Theorem 4.10 of [11] that the equilibrium point $e_1 = 0$ is globally exponentially stable. This shows that the controller is globally exponentially stable for any arbitrary disturbance, given that the disturbance is measurable and bounded. □

Impact of Sensor Failure

The control methodology presented in the main paper relies entirely on the successful operation of a system of distributed pressure sensors. The purpose of this section is to analyze how the system should respond to an individual sensor failure and how the controller would be affected by that failure.

At the start of this analysis, please note that if a sensor module fails, the failure is easily identified. There are two points of failure within the sensor modules: the analog-to-digital converters (ADCs) and the differential pressure sensors. If a sensor fails, the output of the ADC will saturate to either the maximum or minimum digital value. Conversely, during normal operation, the voltage output of the sensors are clamped to a minimum of 5% and a maximum of 95% of the source voltage and the ADC will never measure the minimum or maximum value of its voltage span. Additionally, if the ADC fails, it will stop responding to communication requests, which is easily detected by the central processor.

As a reminder, the algorithm calculating total hydrodynamic force from the differential pressure data assumes that the pressure has a continuous periodic distribution over the AUV surface. The algorithm then fits a series of Fourier coefficients defining the pressure distribution, $\boldsymbol{C_F} = [a_1, a_2, ..., b_1, b_2, ...]^T$, to the measured pressure differentials, $\boldsymbol{\Delta P}$, according to a set of linear equations,

$$\boldsymbol{C_F} = (A_F)^{-1}\,\boldsymbol{\Delta P}\,, \tag{23}$$

where A_F is a matrix defined in the Methods section of the paper. In this experiment, there were two rings of sensors circumscribing the AUV with six sensors each. The Fourier coefficients for three wavemodes are fitted to the six sensor values for each ring. As was mentioned in the Methods section, if a system has more sensors than twice the desired number of wavemodes, then the Fourier fitting is overdetermined and can be used as a filtering process by taking the psuedo-inverse of the matrix A_F which is no longer square.

Similarly, if a sensor (or multiple sensors) are detected to have failed, the algorithm can compensate by reducing the number of desired wavemodes and fitting with the remaining sensors. For such a case, equation (23) will maintain the same form, but the size of the vectors and matrix will change. If one of the sensors fails on the sensor rings in this study, the algorithm can reduce the number of fitted wavemodes to two, using the five good remaining sensors to calculate the total force.

During the experimental trials reported in the study, none of the sensors failed during testing so this algorithm

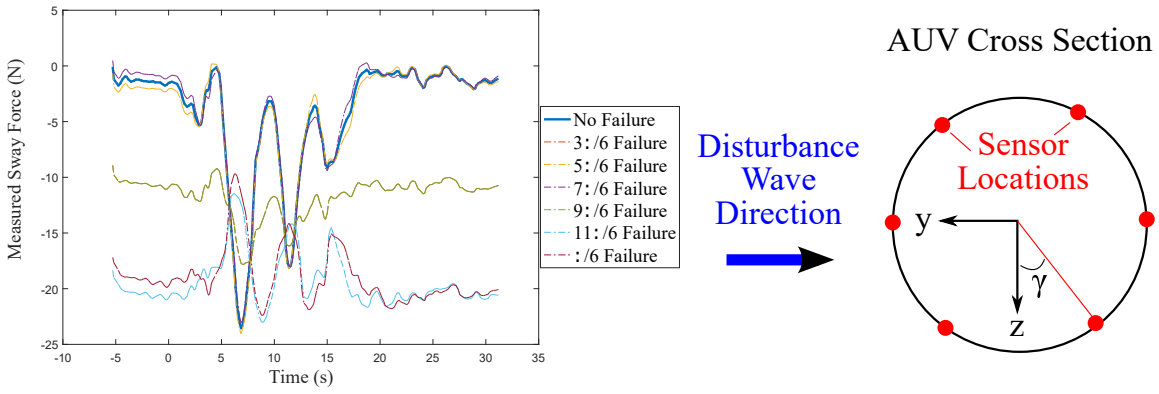

Supplementary Figure 3: The force calculated by a single ring of sensors is shown as a function of time during one of the force feedforward trials for the low frequency disturbance. The thick line shows the force calculated using all six sensors fitting to three wavemodes. The various dash-dotted lines correspond to the force calculated by removing one of the sensors and fitting Fourier coefficients for two wavemodes to the remaining five sensor readings. On the right is a diagram of the definition of sensor angle γ to show the locations of the removed sensor.

Supplementary Table 1: Summary of the control tracking error for different simulated control techniques.

Control	PID	LLFF 10%	LLFF 30%	Sliding 10%	Sliding 30%	Adaptive 10%	Adaptive 30%
Mean Error/D Model (29)a	0.253	0.023	0.034	0.107	0.112	0.202	0.214
RMS Error/D Model (29)a	0.308	0.029	0.042	0.121	0.128	0.244	0.259
Mean Error/D Model (29)b	0.253	0.031	0.040	0.014	0.043	0.037	0.109
RMS Error/D Model (29)b	0.308	0.025	0.050	0.016	0.049	0.046	0.1342
Mean Error/D Model (29)c	0.253	0.015	0.038	0.138	0.135	0.268	0.257
RMS Error/D Model (29)c	0.308	0.020	0.048	0.157	0.154	0.329	0.317

recovery process did not take affect; however, we can use the recorded pressure signals to predict the effect of a sensor failure and response of the recovery process. The data from a single ring of sensors measured during one of the feedforward control cases with a low frequency disturbance was used to calculate the sway force acting on the AUV. The force calculated throughout the trial is shown by the thick solid line in Supplementary Fig. 3. Next, we emulate a sensor failure by removing the data of the failed sensor and calculate the resulting sway force by fitting a Fourier series with two wavemodes to the pressure data of the five remaining sensors. We repeated this calculation for each sensor on the ring; the resulting force calculations are shown in Supplementary Fig. 3. As can be seen, the accuracy of the force calculation is heavily influenced by the location of the failed sensor. If the sensors on the top of the AUV or at the front stagnation point fail there is a negligible effect on the calculated force; however, if the sensors at the rear stagnation point or on the bottom of the AUV fail, then the calculated force becomes unusable which would lead to catastrophic instabilities in the vehicle controller.

It should be noted that the sensory system of this study actually has a fairly sparse sensor distribution, each ring only taking pressure readings at six locations over the entire 360°. Despite the low sensor density the system is still able to accurately measure forces made by unsteady non-uniform disturbance flows. The filtration and Fourier fitting techniques were critical to this accuracy. It should be noted that removing a single sensor from the current setup corresponds to a loss of 16% of the available data, stretching the system to its limits. If the system was intended to be used in a real-world mission, the sensor shell should be designed with more than six sensors per ring, allowing for redundancy in case of individual sensor failure. Additionally, for this particular study, the disturbance flow has little variation along the length of the vehicle, which makes the different sensor rings redundant. Therefore, several sensors could fail on one ring as long as the other ring still has six working sensors. However, this will not be the case for any general disturbance.

Comparison with More Sophisticated Control Algorithms

We chose to compare the experimental performance of the new hydrodynamic force compensation control technique against a basic PD/PID feedback controller because PID feedback control is a standard technique that is well understood. However, there are several more sophisticated control algorithms for systems with nonlinear dynamics that have been used marine robotics. In order to demonstrate how the force compensation control algorithm compares with modern control algorithms and how the lateral line system can be integrated into those algorithms, we created a simulation of a 1D cylindrical AUV and controlled its trajectory using PID, force feedforward, sliding mode, and adaptive sliding mode controllers.

The details of that simulation are presented later in the **Supplementary Methods** section. The AUV is placed in a periodic oscillating uniform background flow, and hydrodynamic forces are calculated from reported data on cylinder drag in cross flow. The lateral line sensory system is also simulated using potential flow solutions to create plausible pressure distributions which are used to calculate pressure differences at the sensor locations. The simulated sensor signals with additional added noise are then used to calculate force according to the Fourier fitting algorithm described in the **Methods** section of the main paper.

The trajectory of the simulated AUV under the different control algorithms is shown in Supplementary Fig.

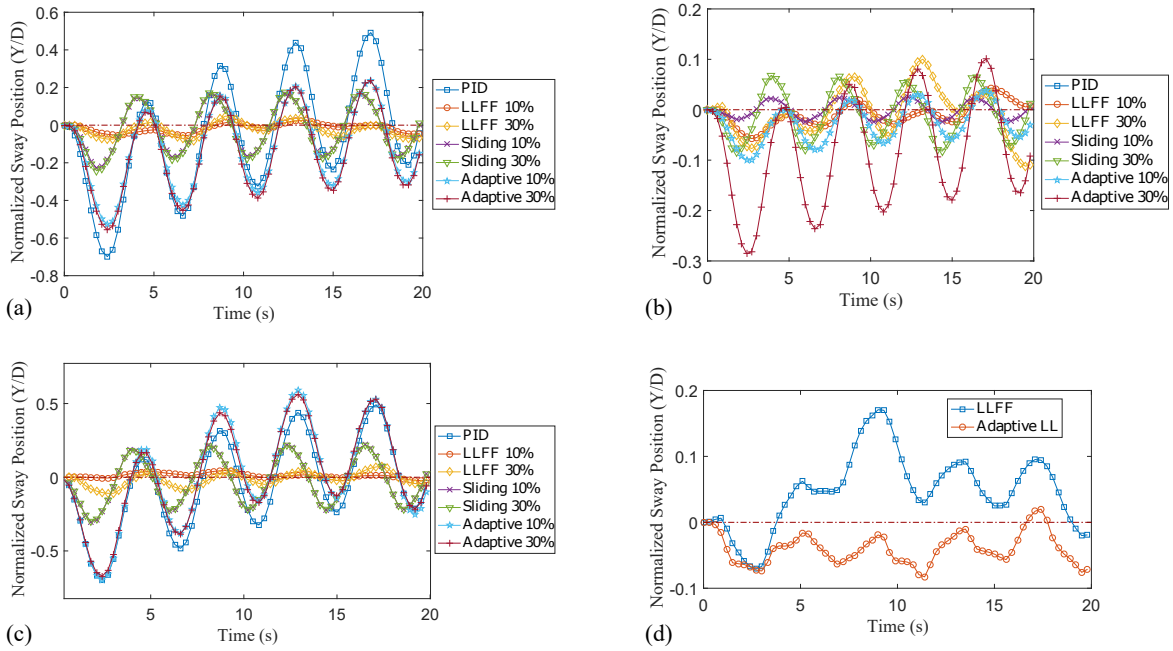

Supplementary Figure 4: Trajectories of the 1D cylinder AUV using various control algorithms in the presence of an oscillating uniform background flow. (a) The controllers assume linear vehicle dynamics and uniform disturbance flow (29)a. (b) The controllers assume nonlinear vehicle dynamics and uniform disturbance flow (29)b, here the PID controller trajectory has been removed so that the relative difference between the other controllers can be seen . (c) The controllers assume nonlinear vehicle dynamics and nonuniform disturbance flow (29)c. (d) A comparison of the lateral line feed forward algorithm compared against an adaptive controller integrating lateral line force measurements (37).

4, and the mean tracking error for each case is reported in Supplementary Table 1. The sliding mode and adaptive sliding mode controllers rely on an estimated vehicle dynamics model, and we have performed simulations using all three versions of the modeled vehicle dynamics summarized by (29) in the **Supplementary Methods**. Additionally, we add error to model coefficients and random Gaussian noise to sensor signals on the order of 10% and 30% of the true value. Since the PID and LLFF controllers do not use estimate models their performance is consistent across the three cases, with the lateral line feedforward technique showing an average improvement over PID control in position tracking of 90% and 85% for the cases with 10% and 30% noise, respectively, which is fairly consistent with experimental testing.

The sliding mode and adaptive controllers show the best performance for the case where disturbances can be considered uniform (with measured relative velocity) and the vehicle dynamics are estimated by nonlinear modeling. For this case both controllers have roughly equivalent performance with the lateral line performance, with the sliding mode performing the best and adaptive sliding mode performing the worst out of the three. For the case where disturbances cannot be considered a uniform background flow, and therefore cannot be measured with a relative velocity, the lateral line feedforward control significantly outperforms the more sophisticated control algorithms, showing a 72% and 85% improvement over the sliding mode and adaptive controllers, respectively, with 30% noise. For this case it should be noted that the adaptive control doesn't show any noticeable improvement over simple PID algorithms.

Finally, we also developed an adaptive control algorithm utilizing the measured hydrodynamic force from the lateral line system, which is summarized in equation (37). The performance of this controller is shown along with the lateral line feedforward control in Supplementary Fig. 4d, with 30% sensor noise for both. The mean tracking error for the lateral line feedforward control is 0.061 vehicle diameters, and the mean tracking error for the adaptive lateral line control is 0.041 diameters, which indicates an additional 33% improvement of the adaptive lateral line control over the basic lateral line feedforward control. It should be noted that this improvement would be even larger if the lateral line sensory system had some form of biased noise in its measurements as opposed to Gaussian noise.

Supplementary Methods

Additional System Validation

This section is used to provide specifics about subsystems and calibration techniques that were not considered essential enough to include in the **Methods** section of the main text.

Lateral Line Sensor Calibration

This subsection provides additional details regarding the calibration of the lateral line system sensor modules.

Before each round of testing, the lateral line was calibrated to ensure the sensors are measuring pressure correctly. After the system was completely submerged underwater, the vehicle was manually positioned in seven different orientations. These orientations were chosen to cover a larger range of roll and pitch orientations than the vehicle was expected to operate during the disturbance rejection test. The vehicle was held fixed at each orientation long enough for the surrounding fluid to come to a steady state. Pressure data was collected in these static flow conditions while the motion capture system was measuring the position and orientation of the vehicle. The roll and pitch angles of the vehicle are used to calculate the vertical separation with respect to gravity of each sensor module; the hydrostatic pressure differences due to this vertical separation is then estimated from supplementary equation (1). Linear regression is used to calculate a best fit line for each sensor module with the slope and offset of the line used to convert the voltage measurements of the ADCs to pressures. These coefficients are then stored in a file which is loaded by the control code during testing. Disturbance rejection testing was then conducted immediately following calibration.

Supplementary Table 2: An example set of calibration coefficients for the sensors on Ring 1. The location of the sensor on the ring is given by the azimuthal angle, γ, which is defined as the angle from the z-axis. The slope and offset are the coefficients of the linear best fit line relating pressure to voltage. The coefficient of determination, or R^2 value, for each set of coefficients is given.

	Sensor 1	Sensor 2	Sensor 3	Sensor 4	Sensor 5	Sensor 6
γ	$\pi/6$	$3\pi/6$	$5\pi/6$	$7\pi/6$	$9\pi/6$	$11\pi/6$
Slope	0.6040	0.6640	0.5580	0.5936	0.6557	0.5758
Offset	2132.1	2121.7	2174.1	2107.3	2176.8	2194.1
R^2	0.9881	0.9494	0.9846	0.9914	0.8311	0.9902

Supplementary Table 3: An example set of calibration coefficients for the sensors on Ring 2. The location of the sensor on the ring is given by the azimuthal angle, γ, which is defined as the angle from the z-axis. The slope and offset are the coefficients of the linear best fit line relating pressure to voltage. The coefficient of determination, or R^2 value, for each set of coefficients is given.

	Sensor 7	Sensor 8	Sensor 9	Sensor 10	Sensor 11	Sensor 12
γ	$\pi/6$	$3\pi/6$	$5\pi/6$	$7\pi/6$	$9\pi/6$	$11\pi/6$
Slope	0.6271	0.5853	0.4813	0.5678	0.5692	0.4110
Offset	2066.6	2161.2	2109.9	2189.2	2114.4	2117.1
R^2	0.9964	0.9008	0.9949	0.9929	0.9311	0.9205

An example set of calibration results for Ring 1 are shown in Supplementary Table 2 and for Ring 2 are shown in Supplementary Table 3. These coefficients were used during several of the high frequency disturbance trials reported in the main text. Supplementary Fig. 5 shows the best fit line to the data points collected by Sensor 4. During this calibration, across all sensors the average coefficient of determination, or R^2 value, for the linear fit line was 0.956 with a standard deviation of 0.052. The high R^2 value suggests that the predicted linear relationship between the measured voltage and corresponding pressure difference is a reasonable fit.

During testing the static component is removed from each sensor's pressure reading, which is calculated from the vehicle orientation as was done for the individual sensor calibration. The pressure signals measured by the both rings of sensors during a passive test are shown in Supplementary Fig. 6a. It is easy to see that the pressure signals are dominated by the static pressure. Supplementary Fig. 6b shows the signals after the static pressure has been removed. Most of the sensors still measure a nonzero pressure at the initial time; this is due to hysteresis on the sensors. We assume that hysteresis is negligible for the duration of a single test, but could potentially have a large build-up over time between different tests. To compensate for hysteresis, we collect pressure data while the vehicle is in stagnant flow conditions for several seconds before each test, and subtract any non-zero dynamic pressure reading from the signal, see Supplementary Fig. 6c. As can be seen, all the processed signals from the pressure sensors remain at nearly zero for several seconds before the disturbance impacts the vehicle. Furthermore, the processed pressure signals begin to converge back onto zero as the disturbance settles, validating the assumption that the hysteresis drift is negligible over a single testing period, and only builds up over larger time scales. For real world applications, sensors with less drift should be selected.

Supplementary Table 4: Roll and pitch angles during the example calibration.

Orientation	1	2	3	4	5	6	7
ϕ	-0.1°	-58.6°	-84.0°	51.7°	84.3°	0.1°	1.5°
θ	0.7°	4.6°	0.9°	5.7°	2.5°	30.7°	-19.4°

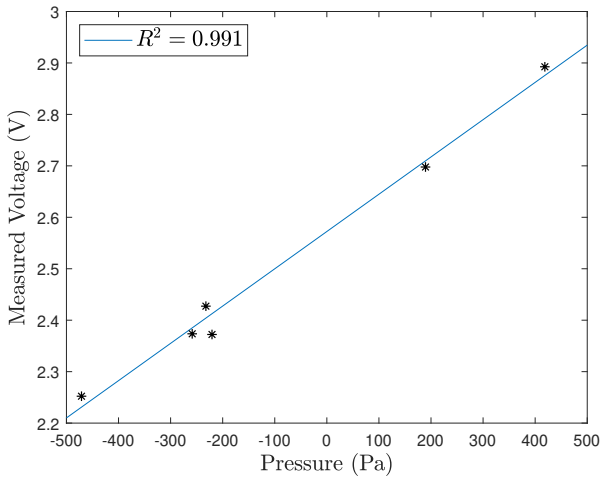

Supplementary Figure 5: Data collected from Sensor 4 located on Ring 1 during calibration showing the relation between the hydrostatic pressure difference and the measured voltage. The sensors exhibit a linear transfer function between pressure and voltage. Linear regression was used to find a best fit line between the data points.

Wave Generator Details

The physical description of the wave generator geometry and kinematics is provided in [12]. Here we provide an additional figure to give graphical representation of the different disturbances generated for this paper. Supplementary Figure 7 shows a scatter plot of the average frequency and amplitude of the wave generator oscillation for each controller case and disturbance condition, as well as error bars to indicate the standard deviations for each case.

Vehicle Control Simulation

We performed experimental testing on the AUV using both standard PD/PID feedback control and the novel lateral line force compensation controller, in order to demonstrate the feasibility of the new technique. As was stated, the PD/PID controller was chosen as a base reference because it is universally understood in the community, and to simplify complications associated with designing more complex controllers for this specific AUV prototype which is not the focus of the current work.

In this section we examine how the new force feedforward technique performs in comparison to more sophisticated control algorithms in simulation, for a cylindrical vehicle with a single degree of freedom. The simulation calculates hydrodynamic forces using nonlinear drag and added mass modeling, and the pressure distribution is calculated from a modified potential flow solution. The lateral line force measurement is also simulated from the modeled pressure distribution allowing us to further investigate the effect of sensor noise on force measurement. Specifically, we operate the virtual vehicle using both sliding mode and adaptive sliding mode controllers since they are common motion control techniques in modern underwater robotic systems. We add a disturbance flow which consists of a periodic oscillation of the background flow.

In the next subsections we will describe the different parts of this simulation in greater detail.

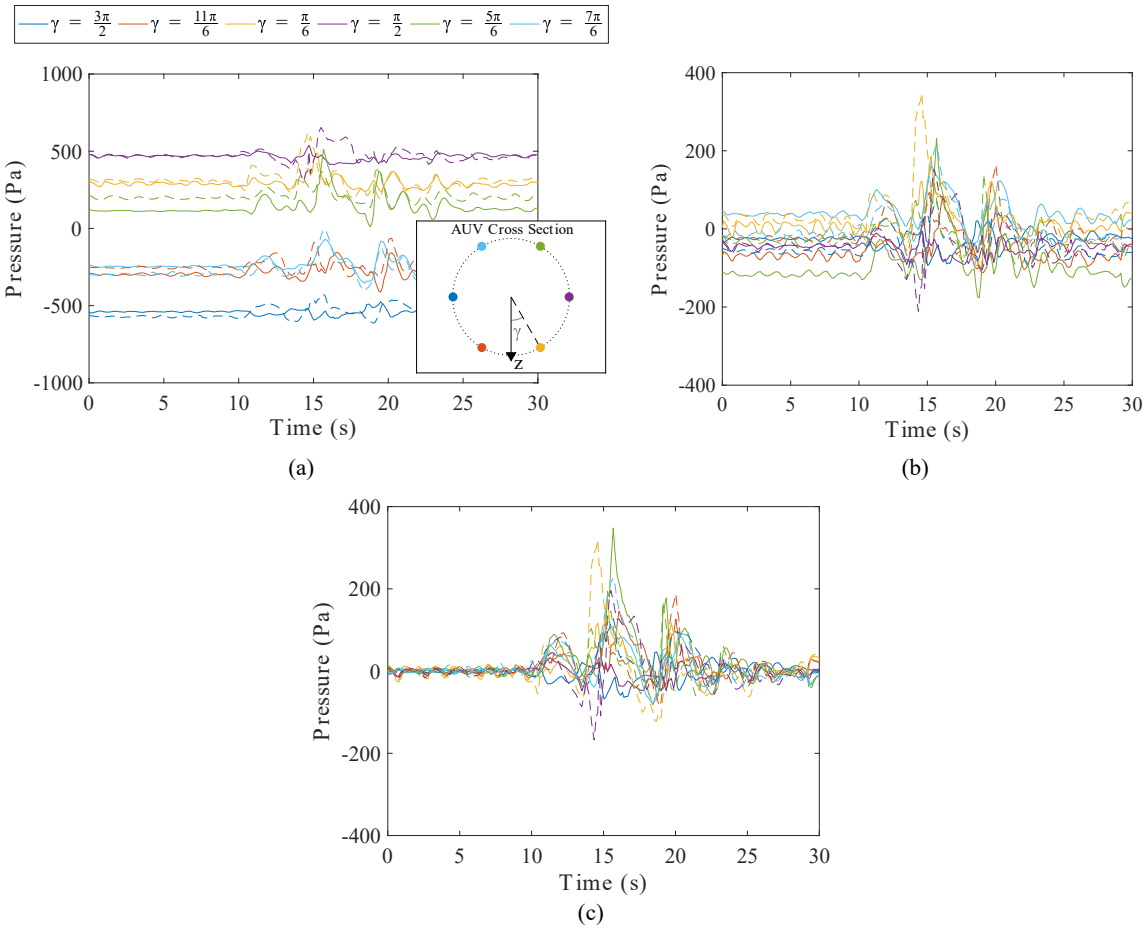

Supplementary Figure 6: (a) Total pressure measured by the twelve ring pressure sensors during a passive test. Solid lines indicate pressure sensors mounted on ring 1 and dashed lines indicate sensors mounted on ring 2. The color of the line indicates the location of the senor module on the respective ring, as shown in the AUV cross-section inset. (b) Dynamic pressure calculated from subtracting the static pressure estimation from the total pressure during a passive test. Several of the pressures are not correctly zeroed by the static pressure compensation indicating that hysteresis is affecting the measurement. (c) Dynamic pressure during a passive test after the hysteresis has been removed from the measurement.

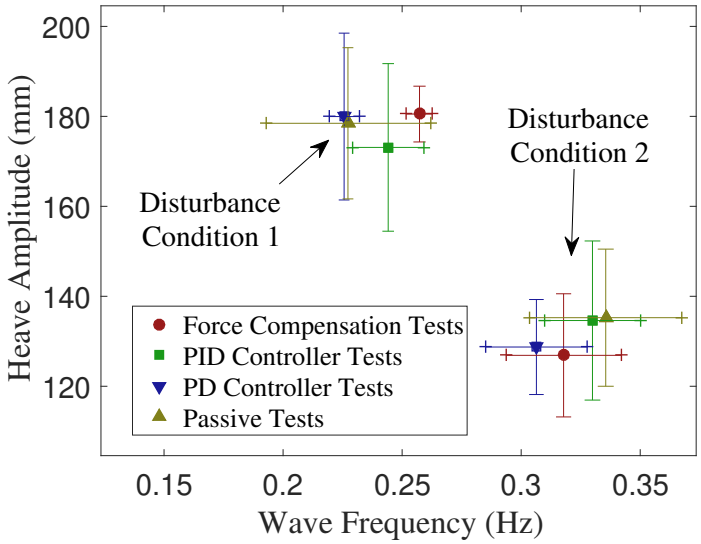

Supplementary Figure 7: Wave generator frequency and amplitude of plate root heaving for each test case of the controllers. The magnitude of the disturbance velocity affecting the vehicle scales with the product of the amplitude and frequency of oscillation of the wave generator.

Vehicle Dynamics

The virtual AUV is a cylinder of equivalent diameter and mass to CephaloBot. It is restricted to motion in the sway (Y) direction, and the vehicle dynamics are given by,

$$(m + m_a)\,\dot{v} = -\frac{\rho}{2} v^2 C_d\,(Re) + F_{dist} + F_c\,, \tag{24}$$

where m is the mass, m_a is the added mass, which is set to one tenth the total mass for this simulation, F_c is the control force, Re is the Reynolds number, $Re = vD/\nu$, and C_d is the Coefficient of drag of a cylinder in cross flow as reported in [13]. F_{dist} is the force due to some fluid disturbance. If the disturbance can be considered large compared to the characteristic vehicle scale, then it can be considered a uniform background flow of velocity U and the forces can be calculated by adding an added mass term, $m_a\dot{U}$ and replacing the vehicle velocity with the relative velocity $v_{rel} = v - U$ in both the drag and Reynolds number calculation. The first type of disturbance we consider is an oscillating ocean current with background flow velocity given by, $U = a_d \sin(2\pi f_d t)$.

The vehicle trajectory over time is integrated numerically between control loop iterations in Matlab using the ODE45 function.

Potential Flow Modeling

In order to simulate the hydrodynamic force measurement using the lateral line system, we need to generate a plausible pressure profile over the surface of the vehicle corresponding to the hydrodynamic forces calculated by the drag modeling. Here we use a modified version of the potential flow over an infinitely long cylinder in a uniform cross flow [14]. The 2D velocity potential at any cross section, $\Phi = -U_p(t)\frac{a^2}{R}\cos(\theta)$, can be used to calculate the pressure on the cylinder surface,

$$P\,(\theta) = P_\infty + \rho\frac{D}{2}\frac{dU_p}{dt}\cos\,(\theta) + \rho U_p^2\left[\cos\,(2\theta) - \frac{1}{2}\right]\,, \tag{25}$$

where P_∞ is the stagnation pressure, U_p is the background flow velocity, and θ is the angular position around the cylinder.

Integration of the unsteady term and multiplying by the length of the vehicle yields the force due to acceleration of the flow (or equivalently acceleration of the body body through stationary fluid, i.e. added mass),

$$\rho\pi \left(\frac{D}{2}\right)^2 L \frac{dU_p}{dt} \,. \tag{26}$$

Since the steady pressure term is symmetric, integration of this profile yields no net force. However, if we add an additional weighted term to the steady pressure and multiply the unsteady pressure term by a scaling coefficient, and replace the potential flow velocity with the relative vehicle velocity, then the modified pressure distribution yields the total hydrodynamic force as used in the vehicle dynamics equation (24).

$$P(\theta) = \frac{m_a}{m}\frac{\rho D}{2}\frac{d(v-U)}{dt}\cos(\theta) + \frac{\rho C_d(Re)}{\pi}(v-U)^2\left[\cos(2\theta) + \cos(\theta) - \frac{1}{2}\right] . \tag{27}$$

This pressure distribution is then used to simulate the difference between pressure at the sensor port locations of the experimental system. Next random Gaussian noise is added to the sensor signals with an amplitude equal to 10% and 30% of the average magnitude of the pressure signals.

The pressure readings are then used to calculate the total hydrodynamic force using the Fourier fitting technique described by equations (11) and (14).

Next we define the different motion control algorithms that will be applied to the vehicle in simulation. We have already defined PID control and hydrodynamic force compensation control in (3) and (4), respectively. We will also define sliding mode and adaptive sliding mode motion control laws to examine through simulation.

Sliding Mode Control

We define a sliding mode controller following the methods of [15, 16]. For sliding mode control we first define a scalar representation of vehicle tracking error for the 1D vehicle,

$$s = \dot{\tilde{Y}} + \lambda\tilde{Y} \,, \tag{28}$$

such that $s = 0$ defines a sliding line in the control space that the vehicle trajectory converges onto, and where λ is the bandwidth of the controller. We define a residual velocity, $\dot{Y}_r = \dot{Y} - s$, for convenience, which converges on the vehicle velocity on the sliding line, and define a Lyapunov function candidate $V = (m + m_a)s^2$. The controller assumes that the vehicle dynamics can be described by a model with a finite number of coefficients. We consider three standard forms of underwater vehicle dynamics models, one is the linear vehicle model which is used to tune control gains, one calculates drag proportional to the relative velocity squared, and the third includes the disturbance force as an independent variable.

$$(m + m_a)\dot{v} = m_a\dot{U} - C(v - U) + F_c \tag{29a}$$

$$(m + m_a)\dot{v} = m_a\dot{U} - C(v - U)^2 + F_c \tag{29b}$$

$$(m + m_a)\dot{v} = -Cv^2 + F_d + F_c \tag{29c}$$

For any disturbance that cannot be considered a uniform background flow (that is, the disturbances that this technology is designed for) equation (29)c must be used. Using these models the rate of change of the Lyapunov

function candidate, $\dot{V} = s\left[(m+ma)\ddot{Y} - (m+ma)\ddot{Y}_r\right]$, can be rewritten as

$$\dot{V} = s\left[m_a\dot{U} - C\left(s + \dot{Y}_r - U\right) + F_c - (m+ma)\ddot{Y}_r\right] \tag{30a}$$

$$\dot{V} = s\left[m_a\dot{U} - C\left(s + \dot{Y}_r - U\right)^2 + F_c - (m+ma)\ddot{Y}_r\right], \tag{30b}$$

$$\dot{V} = s\left[-C\left(s + \dot{Y}_r\right)^2 + F_d + F_c - (m+ma)\ddot{Y}_r\right]. \tag{30c}$$

The rate of change of V can be guaranteed to be negative definite with the control force commanded to

$$F_c = \hat{C}\left(\dot{Y}_r - \hat{U}\right) - \hat{m_a}\dot{\hat{U}} + (m+\hat{m_a})\ddot{Y}_r - k_d s - k_s \tanh\left(\frac{s}{\epsilon}\right), \tag{31a}$$

$$F_c = \hat{C}\left(s + \dot{Y}_r - \hat{U}\right)^2 - \hat{m_a}\dot{\hat{U}} + (m+\hat{m_a})\ddot{Y}_r - k_d s - k_s \tanh\left(\frac{s}{\epsilon}\right), \tag{31b}$$

$$F_c = \hat{C}\left(s + \dot{Y}_r\right)^2 - \hat{F_d} + (m+\hat{m_a})\ddot{Y}_r - k_d s - k_s \tanh\left(\frac{s}{\epsilon}\right). \tag{31c}$$

In these equations the notation $\hat{\cdot}$ refers to an estimate of that quantity, k_d and k_s are sliding mode control gains, where k_s must be selected large enough to overcome uncertainties in model parameters and guarantee the negative definiteness of $\dot{V}$, and ϵ is the thickness of a boundary layer on the sliding line $s = 0$. The term $k_s \tanh\left(\frac{s}{\epsilon}\right)$ is used rather than $k_s sign(s)$ because the smooth and continuous function reduces chattering [16]. The estimate $\hat{U}$ assumes that the vehicle is measuring relative velocity with either an anemometer or laser Doppler sensor, and different levels of uncertainty are added during simulation. It should be noted that for non-uniform disturbances, without a means of sensing the entire flow field $\hat{F_d}$ must be set to 0;

Adaptive Sliding Mode Control

The adaptive sliding mode control, obviously has a similar construct to the sliding mode control. Following the method of [17], we add an additional parameter to the Lyapunov function,

$$V = (m+m_a)s^2 + \tilde{\Theta}^T\Gamma\tilde{\Theta}, \tag{32}$$

where Θ is a vector of the unknown model coefficients $\Theta = [m_a, C]^T$, $\tilde{\Theta} = \hat{\Theta} - \Theta$ is the error between the estimate of the model parameters and the actual values, and Γ is a diagonal weighting matrix, $\Gamma = diag\{\gamma_1, \gamma_2\}$, where both $\gamma_1$and γ_2 are positive constants. Utilizing the same options for vehicle dynamic modeling (29), and a similar control force,

$$F_c = \hat{C}\left(\dot{Y}_r - U\right) - \hat{m_a}\dot{U} + (m+\hat{m_a})\ddot{Y}_r - k_d s, \tag{33a}$$

$$F_c = \hat{C}\left(s + \dot{Y}_r - U\right)^2 - \hat{m_a}\dot{U} + (m+\hat{m_a})\ddot{Y}_r - k_d s, \tag{33b}$$

$$F_c = \hat{C}\left(s + \dot{Y}_r\right)^2 - \hat{F_d} + (m+\hat{m_a})\ddot{Y}_r - k_d s \tag{33c}$$

the rate of change of the Lyapunov function becomes,

$$\dot{V} = -k_d s^2 + \tilde{\Theta}^T\left(s\Phi + \Gamma\dot{\tilde{\Theta}}\right), \tag{34}$$

where Φ is a regressor vector defined by,

$$\Phi = \left[\ddot{Y}_r - \dot{U}, v - U\right], \tag{35a}$$

$$\Phi = \left[\ddot{Y}_r - \dot{U}, (v-U)^2\right], \tag{35b}$$

$$\Phi = \left[\ddot{Y}_r, v^2, -1\right], \tag{35c}$$

It should be noted that, for the first two forms of vehicle modeling (29)a and (29)b, the background flow velocity U must be known to a high degree of accuracy, otherwise the modeled terms in $\dot{V}$ cannot be combined into a linear function of the model parameter error $\tilde{\Theta}$. In addition, for more general vehicle modeling (29)c, the model parameters change to $\Theta = [m_a, C, F_d]$ which is the source of the additional term in (35)c. The rate of change of the Lyapunov function can be made negative definite by assuming stationary model values ($\dot{\Theta} = 0$) and defining an iterative adaptation to the estimated model parameters, $\dot{\hat{\Theta}} = -\Gamma^{-1}\Phi s$, which yields the following iterative adaptations to each of the model parameters,

$$\dot{\hat{m}}_a = -\frac{\ddot{Y}_r - \dot{U}}{\gamma_1} s \,, \qquad \dot{\hat{C}} = -\frac{v - U}{\gamma_2} s \,, \tag{36a}$$

$$\dot{\hat{m}}_a = -\frac{\ddot{Y}_r - \dot{U}}{\gamma_1} s \,, \qquad \dot{\hat{C}} = -\frac{(v - U)^2}{\gamma_2} s \,, \tag{36b}$$

$$\dot{\hat{m}}_a = -\frac{\ddot{Y}_r}{\gamma_1} s \,, \qquad \dot{\hat{C}} = -\frac{v^2}{\gamma_2} s \,, \qquad \dot{\hat{F}}_d = \frac{s}{\gamma_3} \,. \tag{36c}$$

There is an additional special case of adaptive control that we would like to model, whereby the lateral line sensory system is used to provide an estimate of the hydrodynamic forces. We define the vehicle dynamics as simply $m\dot{v} = F_H + F_c$, where F_H is the total hydrodynamic force in the sway direction. We assume that the actual hydrodynamic force is proportional to the measured force, F_m, by some unknown constant, $F_H = C_F F_m$. Defining the sliding mode line s and the Lyapunov function, V, as before, then $\dot{V}$ can be made negative definite by the following control force and model parameter iteration,

$$F_c = -\hat{C_F} F_m + m\ddot{Y}_r - k_d s \,, \tag{37a}$$

$$\dot{\hat{C_F}} = \frac{s F_m}{\gamma_1} \,. \tag{37b}$$

It should be noted that this resulting control force algorithm is nearly identical to that of the force compensation technique defined by (3), with the addition of a term compensating for rigid body inertial forces.

Supplementary References

[1] D. Wang, P. Lermusiaux, P. Haley, *Journal of Marine Systems* **78**, 393 (2009).

[2] T. Lolla, M. P. Ueckermann, P. Haley, *IEEE Conf. on Rob. Autom. (ICRA)* (Minneapolis, USA, 2012).

[3] A. Provenzale, *Ann. Rev. Fluid Mech.* **31**, 55 (1999).

[4] C. Senatore, S. Ross, *American Control Conference* (New York, USA, 2008), p. 1244–1248.

[5] D. Lipinski, K. Mohseni, *Proceedings of the IEEE/RSJ International Conference on Intelligent Robots and Systems (IROS)* (Tokyo, Japan, 2013), pp. 3847–3842.

[6] E. M. Bollt, L. Billings, I. B. Schwartz, *Physica D* **173**, 153–177 (2002).

[7] L. Billings, M. I. Dykman, I. B. Schwartz, *Physical Review E* **78**, 051122 (2008).

[8] C. R. Heckman, I. B. Schwartz, M. A. Hsieh, *Int. J. Rob. Research* **34**, 1590 (2015).

[9] G. Antonelli, *Underwater Robots*, 1610-7438 (Springer, Cham, Switzerland, 2006), chap. 3, pp. 65–100.

[10] J.-E. Slotine, M. D. Benedetto, *IEEE Transactions on Automatic Control* **35**, 848 (1990).

[11] H. K. Khalil, *Nonlinear Systems* (Prentice Hall, Englewood Cliffs, NJ, USA, 2002), third edn.

[12] M. Krieg, K. Nelson, J. Eisele, K. Mohseni, *IEEE Robotics and Automation Letters* **3**, 2378 (2018).

[13] S. F. Hoerner, *Fluid-Dynamic Drag* (Hoerner Fluid Dynamics, Bricktown, NJ, 1965), pp. 3–7 – 3–13.

[14] P. K. Kundu, I. M. Cohen, D. R. Dowling, *Fluid Mechanics* (Academic Press, Waltham, MA, USA, 2011), fifth edn.

[15] D. Yoerger, J. Slotine, *IEEE Journal of Oceanic Engineering* **10**, 462 (1985).

[16] A. J. Healey, D. Lienard, *IEEE journal of Oceanic Engineering* **18**, 327 (1993).

[17] T. I. Fossen, S. I. Sagatun, *Journal of Field Robotics* **8**, 393 (1991).